ACS Catalysis

Research Article

pubs.acs.org/acscatalysis

Theoretical Study of Reaction Mechanism and Stereoselectivity of Arylmalonate Decarboxylase

Maria E. S. Lind and Fahmi Himo*

Department of Organic Chemistry Arrhenius Laboratory, Stockholm University, SE-10691 Stockholm, Sweden

Supporting Information

ABSTRACT: The reaction mechanism of arylmalonate decarboxylase is investigated using density functional theory calculations. This enzyme catalyzes the asymmetric decarboxylation of prochiral disubstituted malonic acids to yield the corresponding enantiopure carboxylic acids. The quantum chemical cluster approach is employed, and two different models of the active site are designed: a small one to study the mechanism and characterize the stationary points and a large one to study the enantioselectivity. The reactions of both α-methyl-α-phenylmalonate and α-methyl-α-vinylmalonate are considered, and different substrate binding modes are assessed. The calculations overall give strong support to the suggested mechanism in which decarboxylation of the substrate first takes place, followed by a stereoselective protonation by a cysteine residue. The enediolate intermediate and the transition states are stabilized by a number of hydrogen bonds that make up the dioxyanion hole, resulting in feasible energy barriers. It is further demonstrated that the enantioselectivity in the case of α-methyl-α-phenylmalonate substrate is dictated already in the substrate binding, because only one binding mode is energetically accessible, whereas in the case of the smaller α-methyl-α-vinylmalonate substrate, both the binding and the following transition states contribute to the enantioselectivity.

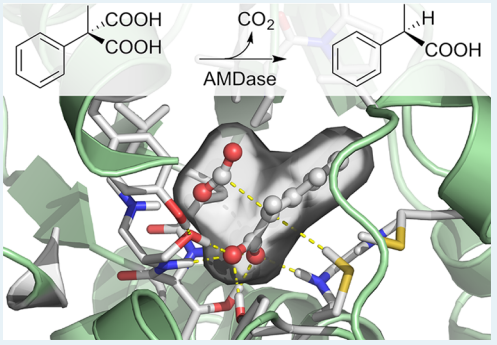

KEYWORDS: *DFT, biocatalysis, enzymology, active site, enantioselectivity, transition state*

I. INTRODUCTION

Arylmalonate decarboxylase (AMDase) from *Bordetella bronchiseptica* catalyzes the asymmetric decarboxylation of α-aryl-α-methylmalonates to give the corresponding enantiomerically pure α-arylpropionates (Scheme 1).[1−4] The products belong

Scheme 1. Reaction Catalyzed by AMDase

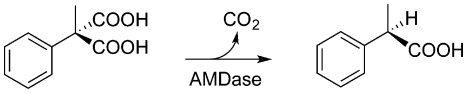

thus to the pharmaceutically interesting group of profens, which are nonsteroidal anti-inflammatory drugs. In contrast to many other decarboxylases, AMDase is independent of cofactors, such as biotin or coenzyme A.[1] These facts make the enzyme of potential interest for use in biocatalytic applications because it provides a way to prepare profen derivatives by enzymatic decarboxylation.[5−8] Interestingly in this context, AMDase also exhibits some aldolase activity toward a properly designed substrate.[9]

The enzyme shows some homology with aspartate and glutamate racemases, in which two cysteine residues are abstracting and delivering an α-proton at the opposite faces of a planar enediolate intermediate.[10,11] For AMDase, a similar two-step reaction mechanism has been proposed (Scheme 2) that involves the formation of the planar enediolate

Scheme 2. Proposed Two-Step Mechanism of AMDase

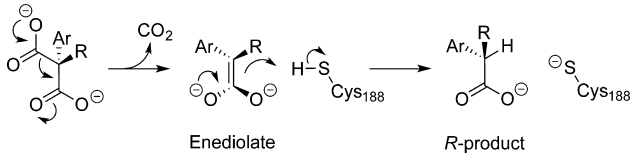

intermediate by decarboxylation of the pro-*R* carboxylate group.[12] The enediolate intermediate is then selectively protonated at the *Si* face by a cysteine residue, resulting in the formation of the *R* enantiomer of the product. Thus, according to this mechanism, the reaction does not involve the formation of a covalent thioester−enzyme intermediate,[12] which has been implicated in some other known decarboxylases and which was also suggested previously for AMDase.[13,14]

The natural substrate of AMDase is unknown, but it has been demonstrated that the enzyme can process many disubstituted malonic acids.[1,3,4,15] The substrate scope is, however, limited to compounds with an aryl or alkenyl group in the α-position.[1,15] Apparently, the substituent must be able to provide some stabilization to the negative charge on the α-carbon in the enediolate intermediate. Moreover, the second α-substituent

Received: July 9, 2014
Revised: October 10, 2014
Published: October 10, 2014

   dx.doi.org/10.1021/cs5009738 | ACS Catal. 2014, 4, 4153−4160

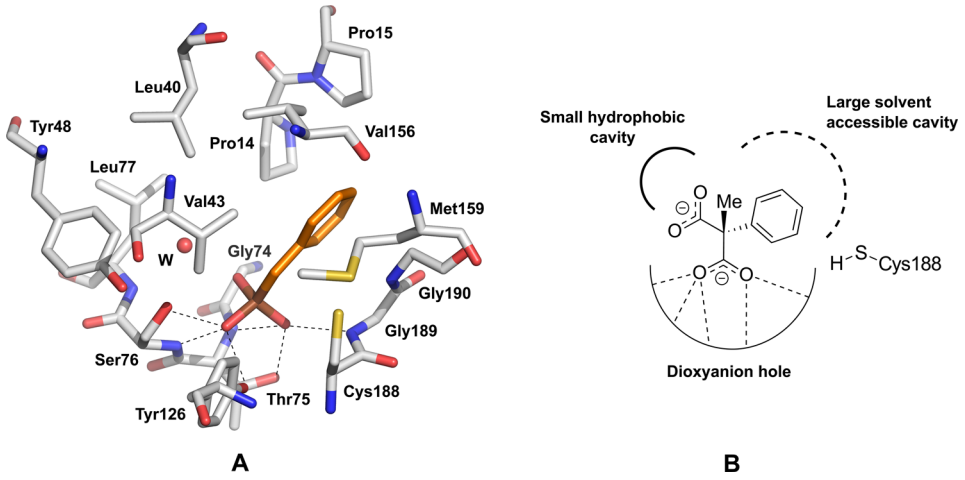

Figure 1. (A) X-ray crystal structure of the active site of AMDase in complex with benzylphosphonate (coordinates taken from PDB 3IP8[15]). (B) Schematic representation of the proposed binding mode of α-methyl-α-phenylmalonate.[15,16]

should not be larger than a methyl group to be properly accommodated in the active site.[1,3] Hence, both steric and electronic factors influence the substrate scope of the enzyme.

A number of X-ray crystal structures of AMDase have been solved in recent years.[15−18] The enzyme consists of two domains, each containing a four-stranded parallel β-sheet with α-helices on both sides, and the active site is located in a cleft between two β-strands. Very importantly, the high-resolution structures showed that the active site contains two adjacent oxyanion holes (referred to as dioxyanion hole) that can donate six hydrogen bonds to bind a carboxylate group of the substrate and provide stabilization to the enediolate intermediate.[15,16] The structures also established that the AMDase active site has two cavities, one large solvent-exposed and one small hydrophobic.[15,16] Modeling of the enediolate intermediate docked into the active site[16] and a subsequent structure cocrystallized with the mechanism-based inhibitor benzylphosphonate that resembles the enediolate[15] have shown that the phenyl group is positioned in the larger pocket (Figure 1A). On the basis of these findings, it has been suggested that the substrate binds to the active site with the large substituent in the large solvent-accessible pocket and the leaving pro-*R* carboxylate group in the small hydrophobic pocket (Figure 1B).[15,16] The negative charge on the pro-*S* carboxylate group is stabilized by hydrogen bonds to the dioxyanion hole. According to this scheme, upon decarboxylation, the resulting enediolate intermediate will be protonated at the *Si* face by Cys188 to yield the *R* product. Thus, if no rearrangement of the intermediate takes place during the reaction, the location of this cysteine residue with respect to the substrate will be decisive for the stereochemical outcome.

The importance of Cys188 has been demonstrated by site-directed mutagenesis, where the Cys188Ser mutant showed a drastic decrease in rate constant (k_{cat}).[19] Introducing another cysteine residue at the *Re* face of the intermediate (by the Gly74Cys mutation) resulted in a mutant with racemization activity,[20,21] whereas the Gly74Cys/Cys188Ser double mutant showed the opposite stereoselectivity compared with the wild-type enzyme.[18,22,23]

In other relevant mechanistic studies, ^{13}C and ^{18}O isotope-labeling experiments have confirmed that the decarboxylation occurs through elimination of the pro-*R* carboxylate group and also showed that the *R* product is formed with inversion of configuration of the α-carbon.[13,16] Furthermore, no kinetic isotope effects were observed in experiments carried out in deuterated water, which suggests that decarboxylation is the rate-limiting step.[24]

In the present study, we use density functional theory (DFT) calculations to investigate the reaction mechanism and stereoselectivity of AMDase. Detailed knowledge of the mechanism and the roles of the various residues in the active site is important for further protein engineering with the aim of producing an enzyme with improved stereoselectivity for an extended substrate scope. For this purpose, we have designed two different models of the active site on the basis of the high-resolution structure of AMDase, cocrystallized with benzylphosphonate (PDB 3IP8[15]). The first contains only parts of the residues constituting the dioxyanion hole and the Cys188 residue (model I, 81 atoms), and the second includes additional active site residues that define the small and large binding pockets (model II, 223 atoms). As a substrate, α-methyl-α-phenylmalonate (methylphenylmalonate) has been used. To further study the stereoselectivity of the enzyme, we have for the larger model also considered another substrate, α-methyl-α-vinylmalonate (methylvinylmalonate) because the vinyl group is considerably smaller in size compared with a phenyl, which could have implications on the stereoselectivity.

II. COMPUTATIONAL DETAILS

All calculations were performed with the B3LYP hybrid density functional method[25,26] as implemented in the Gaussian03 program package.[27] Geometries were optimized using the 6-31G(d,p) basis set, and more accurate energies were obtained by single-point calculations on the optimized geometries employing the larger 6-311+G(2d,2p) basis set. Solvation effects were computed at the same level of theory as the geometry optimizations by single-point calculations on the optimized structures using the conductor-like polarizable continuum model.[28,29] In this model, the solute is embedded in a cavity surrounded by a homogeneous polarizable medium with some dielectric constant (ε), which in the present calculations is set to 4. Calculation using the higher dielectric constant ε = 80, representing water solution, have also been performed, and the results are reported in the Supporting Information. The differences in the energy profiles between the two dielectric constants are rather small. Frequency calculations

dx.doi.org/10.1021/cs5009738 | ACS Catal. 2014, 4, 4153−4160

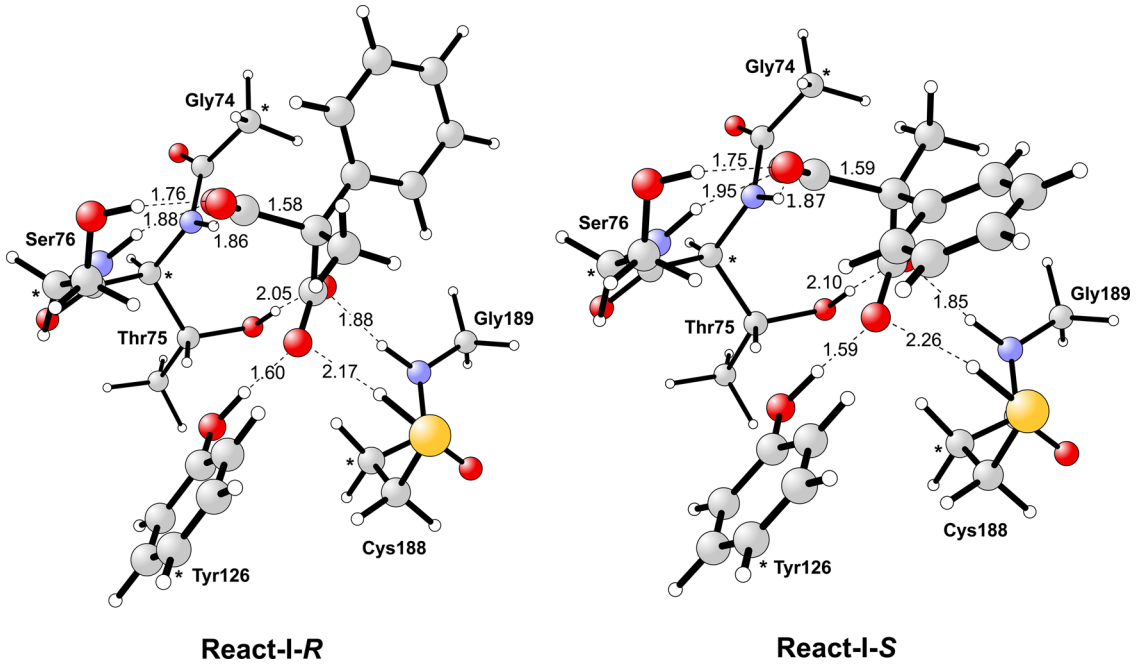

Figure 2. Optimized structures of the two enzyme–substrate complexes in model I. Distances are given in angstroms. Fixed atoms are shown by an asterisk.

were carried out at the same theory level as the geometry optimizations to confirm the nature of the stationary points and to obtain zero-point energy (ZPE) corrections.

A known problem in the many density functionals (e.g., B3LYP) is the lack of a proper description of the attractive long-range dispersion interactions. To correct for this, an empirical correction term is added to the energy according to the DFT-D2 method.[30] Recently, this correction has become more frequently employed in similar applications.[31−35]

To prevent unrealistic movements of the residues during the geometry optimizations, a number of atoms were locked to their crystallographic positions. This is a standard procedure used previously in many applications of the cluster approach for enzyme modeling.[36,37] By doing so, some imaginary frequencies are introduced, in this case, all below 60*i* cm^{-1}. These frequencies have no impact on the ZPE but render the entropy calculations unreliable.

In general, entropy effects are rather small in the chemical steps of enzymatic reactions; that is, when there is no binding or release of substrates or products.[38−40] It is therefore a rather good approximation to simply ignore the entropy in the cluster approach. However, in cases where a gas molecule binds or is released during the reactions, as is the case in the decarboxylation reaction considered here, the entropy effect becomes very significant and has to be considered. In accordance with previous quantum chemical studies of enzymes in which small gas molecules are released,[41] the entropy gain when CO_2 is released is estimated to be equal to the translational entropy for the free molecule, which here is calculated to be 11.1 kcal/mol at room temperature. This value is thus added to the reaction energy of the first step of the AMDase reaction.

The final energies reported in the present paper are thus the large basis set energies corrected for ZPE, solvation, and dispersion effects. Only the energy of the decarboxylation step has been corrected for the entropy effect according to above.

III. RESULTS AND DISCUSSION

III.A. Active Site Model I. First, a smaller model of the AMDase active site was constructed consisting only of the residues proposed to be parts of the dioxyanion hole (namely, Gly74, Thr75, Ser76, Tyr126, and Gly189[15,16]) together with Cys188, which is responsible for the protonation (see Figure 2). The model consists of 81 atoms and has a total charge of −2, which is the charge of the fully deprotonated methylphenylmalonate substrate. Truncations were made at the *α*-carbons of the amino acids, except for tyrosine, which was modeled as a phenol. This model lacks the residues that define the two cavities discussed above, and it is therefore not expected to reproduce or rationalize the stereoselectivity. However, it still provides important information regarding the reaction mechanism and the involved transition states and will serve for comparison purposes with the extended model II below.

The substrate was manually placed in the active site model, and different orientations of the small and large substituents and different hydrogen bonding patterns to the two carboxylate groups were considered. The calculations show that the lowest-energy binding modes have both carboxylates bound to the dioxyanion hole by six hydrogen bonds, three to each carboxylate moiety (see Figure 2). It is interesting to note that also the Cys188 residue interacts with the pro-*S* carboxylate of the substrate with a weak hydrogen bond.

The proposed enzyme–substrate complex corresponding to Figure 1B, in which only the pro-*S* carboxylate group is bound to the dioxyanion hole,[15,16] could not be optimized. All attempts to obtain such geometry converged to a structure in which both carboxylate groups form hydrogen bonds with the dioxyanion hole. It can be argued that the lack of the small and large cavities in this model might be the reason for this. However, as will be discussed in next section, a binding pattern similar to that in Figure 2 is also observed in the large model.

dx.doi.org/10.1021/cs5009738 | *ACS Catal.* 2014, 4, 4153−4160

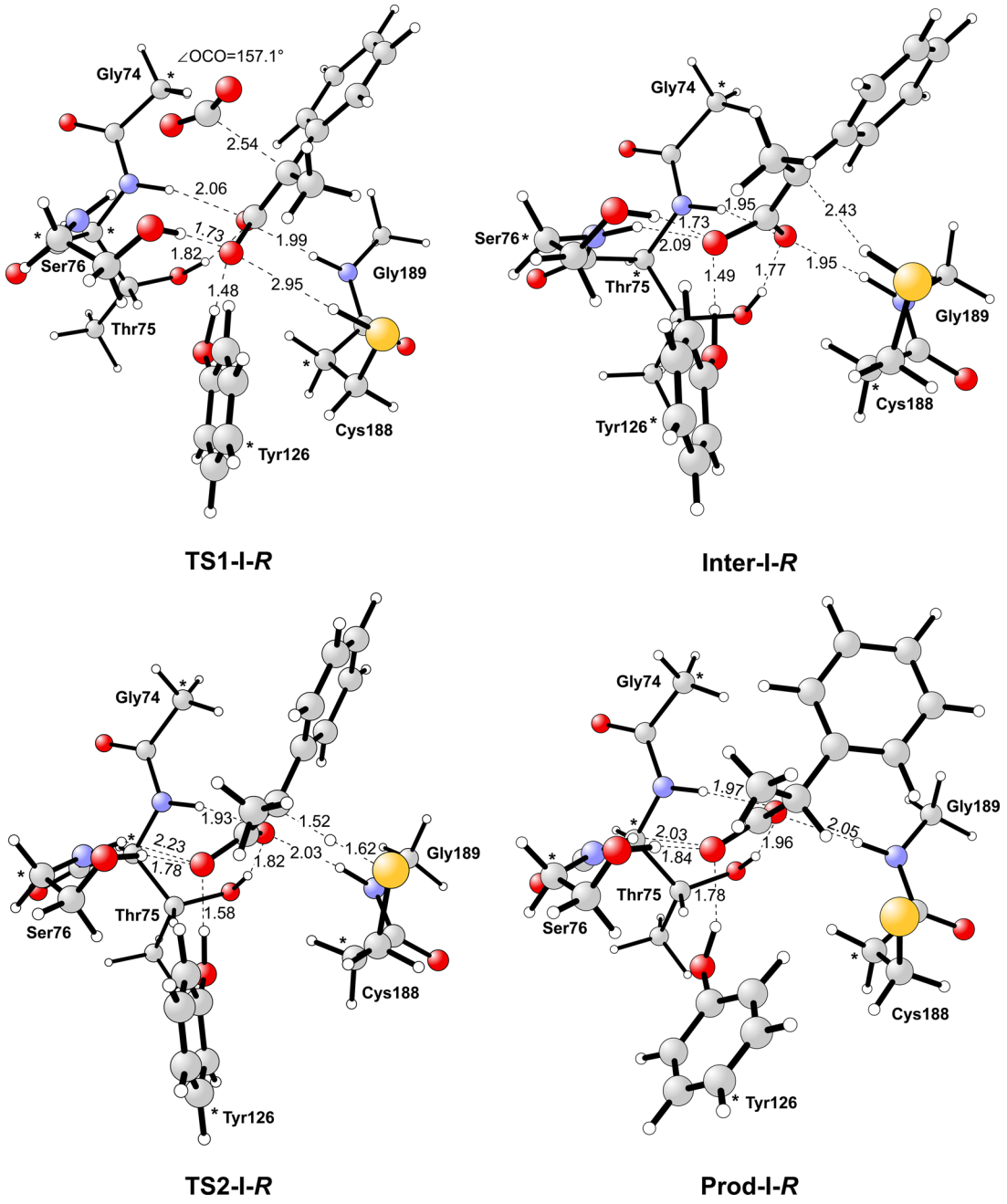

Figure 3. Optimized stationary points for the decarboxylation according to binding mode React-I-*R* in model I.

The two enzyme−substrate complexes found for model I (Figure 2) differ in the positions of the small and large substituents. They are termed React-I-*R* and React-I-*S* because after decarboxylation (of the pro-*R* carboxylate in the former and the pro-*S* carboxylate in the latter), they result in the *R* or the *S* forms of the final product, respectively. Quite expectedly, because of the lack of the small and large cavities in this small model, the two enzyme−substrate complexes are close in energy, differing only by 1.9 kcal/mol in favor of React-I-*R*.

Starting from React-I-*R*, the transition state for the decarboxylation of the pro-*R* carboxylate (TS1-I-*R*) and the resulting enediolate intermediate (Inter-I-*R*) were then optimized and are shown in Figure 3. The barrier is calculated to be 19.5 kcal/mol, and the reaction energy of the step is +9.3 kcal/mol, including the entropy correction discussed above in the Computational Details section. In TS1-I-*R*, all hydrogen bonds of the dioxyanion hole are now oriented toward the enediolate, except for the Thr75-Ser76 backbone amide. We also note that most of the hydrogen bonds to the carboxylate oxygens are shortened in the TS and further in the intermediate, indicating that they stabilize the charge developing on the enediolate. In Inter-I-*R*, the carboxylate of the enediolate intermediate is bound by six hydrogen bonds to the dioxyanion hole, resembling very well the X-ray crystal structure.[15]

Here it should be noted that we also attempted to find the transition state for the decarboxylation of the pro-*S* carboxylate from React-I-*R*. However, from a linear transit scan of the C−C bond, it turns out that the barrier for decarboxylation is more than 20 kcal/mol higher compared to the pro-*R* counterpart. This is of course because the pro-*S* carboxylate is buried inside the dioxyanion hole. This result is consistent with the isotope

dx.doi.org/10.1021/cs5009738 | *ACS Catal.* 2014, 4, 4153−4160

labeling experiments showing that the decarboxylation occurs through elimination of the pro-*R* carboxylate.[13,16]

In Inter-I-*R*, Cys188 is located in a good position for delivering the proton to the *Si* face of the enediolate intermediate. We have optimized the transition state for this proton transfer (TS2-I-*R*) and the resulting product complex (Prod-I-*R*) (see Figure 3). In these calculations, the CO_2 gas has been removed from the model. From Inter-I-*R*, the calculated barrier for the proton transfer is 3.5 kcal/mol (i.e., 12.8 kcal/mol relative to React-I-*R*), and the step is exothermic by 13.0 kcal/mol.

The overall calculated energy profile is presented in Figure 4 and shows that the decarboxylation step is rate-limiting, in

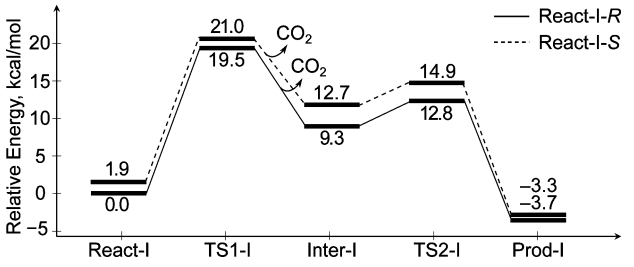

Figure 4. Calculated energy profile for model I with methylphenylmalonate substrate.

accordance with the experimental findings.[24] The calculated barrier (19.5 kcal/mol) is somewhat overestimated compared with the experimental estimations of 14−16 kcal/mol, which can be deduced from the measured k_{cat} values of 30 and 279 s^{-1} for the decarboxylation of methylphenylmalonate.[1,42,15]

The corresponding energy profile was also calculated for the other binding mode (i.e. starting from React-I-*S*) and is shown in Figure 4. In this case, the decarboxylation occurs at the pro-*S* carboxylate leading to the final *S* product. The optimized structures of the stationary points are given in the Supporting Information (SI). As expected, this model cannot fully reproduce the enantioselectivity of AMDase. The calculated energies for the two binding modes are very close, since the model is small and lacks the important binding pockets. The energy difference in the rate-limiting step between formation of the *S* and *R* product is only 1.5 kcal/mol. Experimentally, methylphenylmalonate is converted with an enantiomeric excess (ee) of >99%,[1] which corresponds to an energy difference of at least 3 kcal/mol.

One final mechanistic detail should be mentioned here. Recent calculations on the above-mentioned glutamate racemase enzyme have suggested that the deprotonation and protonation of the substrate occur in a single concerted step.[43] Therefore, we have in the present study also considered whether decarboxylation and protonation could occur simultaneously in AMDase. However, no such transition state could be located, as all attempts to optimize a concerted TS converged into TS2. This suggests that the reaction is a stepwise one.

To summarize this part, the results of model I give general support to the previously suggested reaction mechanism of

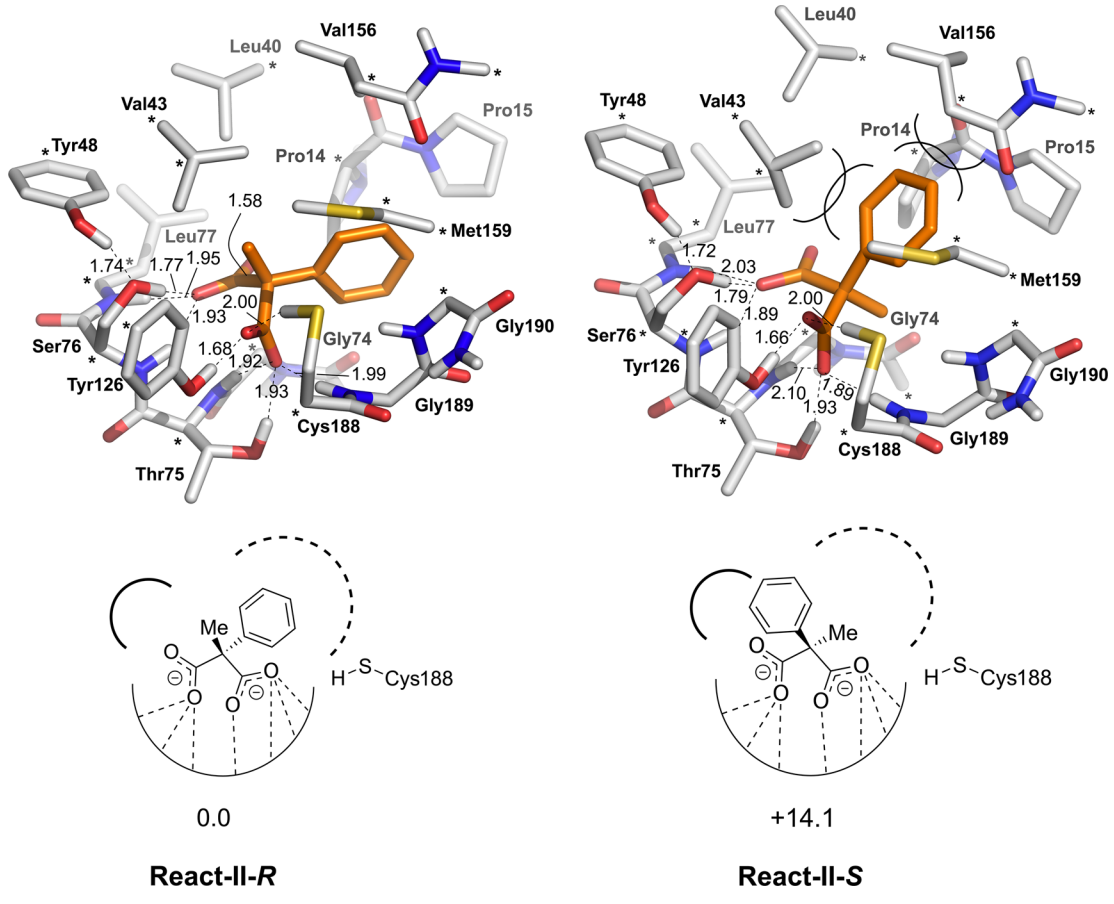

Figure 5. Optimized structures and schematic drawings of the React-II-*R* and React-II-*S* binding modes of the methylphenylmalonate substrate to model II. The calculated relative energies (kcal/mol) are indicated.

dx.doi.org/10.1021/cs5009738 | *ACS Catal.* 2014, 4, 4153−4160

Scheme 2. However, this model is too small to rationalize the enantioselectivity of AMDase. More realistic representation of the active site is necessary for that, as will be demonstrated by model II below.

III.B. Active Site Model II. In the large model II, the residues constituting the small and large cavities were included in addition to the groups of model I. These additional groups are Pro14, Pro15, Leu40, Val43, Tyr48, Val156, Met159, and Gly190. Examination of the active site showed that the backbone peptide bond between Ser76 and Leu77 might be a part of the hydrogen-bonding network. Therefore, the latter amino acid was also included in the model. Furthermore, the peptide bond between Met73 and Gly74 was also kept in the model. In the crystal structure with the phenylphosphonate inhibitor,[15] there is a water molecule in the active site within hydrogen bonding distances to the side chain of Ser76 and the Ser76-Leu77 backbone amide (Figure 1A). When the substrate was placed in the active site, we found that one of its carboxylates would take the position of this water (see Figure 5); therefore, the water was not included in the model. However, it cannot be excluded that a water molecule can enter the active site at a later stage of the reaction. This has not been considered explicitly in the current investigation.

The resulting active site model consists thus of 223 atoms using methylphenylmalonate as a substrate. Also for this model, the total charge is −2, which is the charge of the fully deprotonated substrate. As before, truncations of the various groups were made, as shown in Figure 5.

The methylphenylmalonate substrate was placed in the active site of model II, and a number of different binding modes were considered. Similarly to the smaller model, the binding mode that turned out to have the lowest energy, React-II-*R*, has both carboxylates bound to the dioxyanion hole (see Figure 5). In this model, the peptide bond between Ser76 and Leu77 forms an additional hydrogen bond to the substrate, which is now bound by seven hydrogen bonds to the dioxyanion hole. In addition, the Cys188 residue has an interaction with the substrate, as was the case in the small model. The phenyl substituent is positioned in the large solvent accessible cavity, whereas the methyl substituent points toward the small space enclosed by Val43. Although seemingly different, this binding mode is, in fact, quite similar to the one proposed previously on the basis of the high-resolution crystal structure shown schematically in Figure 1B.[15,16] The difference is that the pro-*R* carboxylate tilts away somewhat from the hydrophobic pocket to form hydrogen bonds to the dioxyanion hole.

The other binding modes have significantly higher energies compared to React-II-*R*. For example, React-II-*R*1, in which the pro-*R* carboxylate and the methyl substituent change places resulting in only the pro-*S* carboxylate being bound to the dioxyanion hole (see SI for optimized structure) is 11.7 kcal/mol higher than React-II-*R*. Another binding mode, React-II-*R*2, in which only the pro-*S* carboxylate is bound to the dioxyanion hole while the pro-*R* carboxylate points into the hydrophobic pocket, results in the pro-*S* carboxylate being bound only by three hydrogen bonds and is as much as 22.1 kcal/mol higher than React-II-*R* (see SI). Attempts to optimize similar structures in which the pro-*S* carboxylate is bound by more hydrogen bonds to the dioxyanion hole converged to structures very similar to React-II-*R*.

Importantly for the enantioselectivity of the reaction, a binding mode that would lead to the *S* form of the product is React-II-*S*, shown in Figure 5. Similarly to React-II-*R*, both carboxylates are bound to the dioxyanion hole, but now with the phenyl and methyl substituent changing places. That is, the methyl group points toward the solvent-accessible pocket, and the phenyl group points somewhere between the hydrophobic pocket and the area next to it. The energy of this complex is 14.1 kcal/mol higher than React-II-*R*. This large energy difference is caused mainly by the steric clash between the large substituent and the side chains of Leu40, Val43, and Val156, which are parts of the small hydrophobic binding pocket. Thus, already at the binding of the substrate, we can see that the active site causes a large discrimination between the two binding modes that lead to the two different enantiomers of the final product.

Here, it should be pointed out that the calculated energy differences between the various binding modes could be somewhat overestimated due to the constraints imposed in the model. That is, if even larger and more flexible models of the cavities are used, it might lead to somewhat smaller energy differences because the active site cavities might be able to expand or shrink somewhat to better accommodate the substituents.

Next, starting from the lowest-energy binding mode that leads to the *R* product (React-II-*R*) and the binding mode that leads to the *S* product (React-II-*S*), we optimized the transition states and intermediates for the following steps in the reaction. The calculated energies are shown in Figure 6, and the optimized geometries are given in the SI.

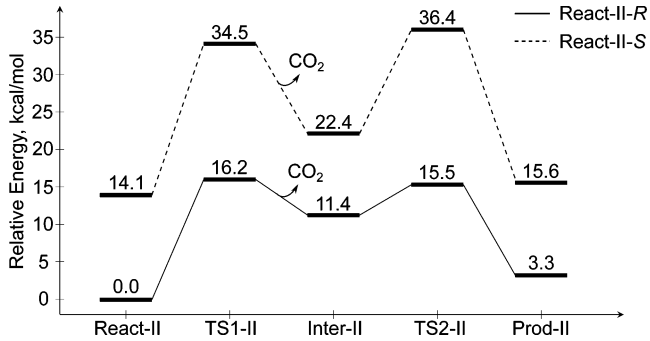

Figure 6. Calculated energy profile for model II and with the methylphenylmalonate substrate starting from either React-II-*R* or React-II-*S*.

For the formation of the *R* product, the energy profile is quite similar to the one found for model I. One small difference is that the barrier for the rate-limiting decarboxylation step (TS1-II-*R*) now is calculated to be 16.2 kcal/mol, which is ∼3 kcal/mol lower than for the smaller model.[44] This barrier is thus in better agreement with the experimental values of 14−16 kcal/mol.[1,15,42] One contributing factor could be the extra hydrogen bond in TS1 of model II between the Thr75-Ser76 backbone amide and the carboxylate group. This hydrogen bond is not observed in TS1 of model I. Another small difference is that both the enediolate intermediate (Inter-II-*R*) and the following transition state (TS2-II-*R*) and product complex (Prod-II-*R*) are somewhat higher in energy. Thus, inclusion of more groups at the active site makes the planar intermediate and the inversion of the carbon center somewhat less stable.

The energy profile corresponding to the formation of the *S* product, on the other hand, is drastically different compared with model I. The barrier for the decarboxylation (TS1-II-*S*) is now as high as 34.5 kcal/mol, which is 18.3 kcal/mol higher

dx.doi.org/10.1021/cs5009738 | ACS Catal. 2014, 4, 4153−4160

than for the *R* product. The large difference in the binding energies is thus enhanced even more because the planar structure of the enediolate intermediate causes even more steric clash between the large substituent and the residues of the small cavity. A planar conformation is not possible when the phenyl ring is situated in the smaller cavity, and therefore, the substrate is forced further out of the active site to be able to attain a planar conformation. As a result, the hydrogen bonds to the side chain of Ser76 and to the Thr75-Ser76 backbone amide are lost. We note also that a proton is transferred to the substrate from Tyr126, whose negative charge now is stabilized by a hydrogen bond to the side chain of Ser76 (see SI for optimized structures). In the protonation step (TS2-II-*S*), the difference in energy between the two binding modes becomes even larger (20.9 kcal/mol) because the inversion of the carbon causes more steric repulsion between the large substituent and the small cavity.

Overall, the results of the large model II corroborate the results of the smaller model I in showing that the proposed mechanism of Scheme 2 is energetically plausible. The large model further establishes that the substrate binds such that the two carboxylates are bound to the dioxyanion hole. The very large energy difference between the energy profiles for the paths leading to the different enantiomers of the product shows that the formation of the *R* product will be exclusive, which is consistent with the experimental finding of ee being >99%.[1] According to this model, the stereochemical outcome for this substrate is determined already at the binding of the substrate because the large phenyl substituent fits quite badly in the small binding pocket, causing the energies of both the binding and the following transition states to be much higher for the formation of the *S* enantiomer.

The results of model II can also be used to qualitatively rationalize the stereochemical outcome of the Gly74Cys/Cys188Ser double mutant. As discussed in the Introduction, it has been shown that this mutant yields the opposite enantioselectivity compared with the wild type.[18,22,23] Assuming that the two point mutations do not significantly affect the energy difference between the different binding modes, then also for this mutant, the pro-*R* carboxylate will dissociate in the first step. The position of the cysteine residue, which in the mutant will be located at the *Re* face of the enediolate intermediate, will in the second step determine the stereochemistry of the final product, thus yielding the *S* enantiomer.

III.C. Methylvinylmalonate Substrate. To further investigate the enantioselectivity of AMDase, we now turn to a substrate with a much smaller substituent than phenyl, namely methylvinylmalonate. For this substrate, the experiments show that the rate constant is ∼1 order of magnitude lower compared with methylphenylmalonate, and the ee is 99%, still in favor of the *R* product.[15]

Model II was used, and the stationary points for the reactions of binding modes React-II-*R* and React-II-*S* were optimized. The outcome in terms of calculated energy profiles is shown in Figure 7, and the optimized geometries are given in the SI.

We note first that the overall calculated rate-limiting barrier for this substrate is 15.4 kcal/mol, which is slightly lower than for the methylphenylmalonate substrate (Figure 6). According to above, the experimental trend should be the opposite: that is, the barrier for methylvinylmalonate should be somewhat higher than for methylphenylmalonate. As discussed earlier, this might indicate that the models of the small and large cavities could be a bit too small and rigid. A substantially larger model might be able to reproduce this trend by allowing the binding pocket to adapt properly to the substituents.

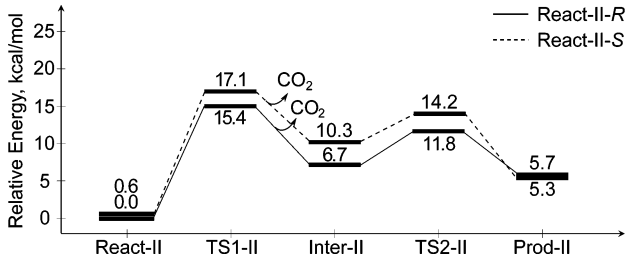

Figure 7. Calculated energy profile for model II with methylvinylmalonate substrate.

In the case of methylvinylmalonate substrate, the two binding modes now are much closer in energy. The energy of React-II-*S* is only 0.6 kcal/mol higher than React-II-*R*. As expected, the vinyl substituent can be much better accommodated into the smaller cavity as compared with the phenyl substituent in the case of the methylphenylmalonate substrate. This is a very interesting result that indicates that the stereoselectivity in this case is not entirely determined in the binding of the substrate. Instead, in the following rate-determining decarboxylation transition state (TS1), the energy difference increases to 1.7 kcal/mol. As before, although less pronounced, the energy difference stems from steric clash between the vinyl substituent and the residues of the small cavity. The calculated difference in barriers is underestimated compared with the experimental findings, since, as stated above, an ee of 99% should correspond to at least 3 kcal/mol. Again, a much larger model with more flexible binding pockets might result in a better agreement regarding the enantioselectivity of this substrate.

IV. CONCLUSIONS

In the present paper, we have used density functional theory calculations to investigate the reaction mechanism of AMDase. Two models of the active site are devised on the basis of the crystal structure. The smaller model (81 atoms) is first used to study the reaction mechanism and characterize the involved transition states and intermediates. It is shown that the previously suggested two-step mechanism, involving decarboxylation of the substrate and stereoselective protonation of the resulting enediolate intermediate by the Cys188 residue, is energetically plausible. However, this model cannot fully reproduce or rationalize the enantioselectivity of the enzyme. A larger model consisting of 223 atoms is therefore designed in which a number of groups constituting the small and large substrate binding pockets are included. Two representative substrates are considered, methylphenylmalonate and methylvinylmalonate, and different substrate binding modes are evaluated. In the case of methylphenylmalonate, the calculations show that the large phenyl substituent causes a large energy difference between the binding modes, which indicates that the enantioselectivity is determined already at the binding of the substrate. However, in the case of methylvinylmalonate, which has a considerably smaller substituent, the energy difference between the binding modes is small and the calculations suggest that also the decarboxylation transition state contributes to the enantiodiscrimination.

dx.doi.org/10.1021/cs5009738 | *ACS Catal.* 2014, 4, 4153−4160

■ ASSOCIATED CONTENT

Supporting Information

Additional figures of optimized structures for models I and II. Cartesian coordinates of all presented structures. This material is available free of charge via the Internet at http://pubs.acs.org.

■ AUTHOR INFORMATION

Corresponding Author

*E-mail: himo@organ.su.se.

Notes

The authors declare no competing financial interest.

■ ACKNOWLEDGMENTS

We acknowledge financial support from the Swedish Research Council, the Göran Gustafsson Foundation, and the Knut and Alice Wallenberg Foundation. Computer time was generously granted by the Swedish National Infrastructure for Computing.

■ REFERENCES

(1) Miyamoto, K.; Ohta, H. *Eur. J. Biochem.* **1992**, *210*, 475−481.
(2) Miyamoto, K.; Ohta, H. *Appl. Microbiol. Biotechnol.* **1992**, *38*, 234−238.
(3) Miyamoto, K.; Ohta, H. *Biocatalysis* **1991**, *5*, 49−60.
(4) Miyamoto, K.; Ohta, H. *J. Am. Chem. Soc.* **1990**, *112*, 4077−4078.
(5) Ohta, H. In *Advances in Biochemical Engineering/Biotechnology*; Faber, K., Ed.; Springer: Berlin, Heidelberg, 1999; Vol. *63*, pp 1−30.
(6) Kourist, R.; Domínguez de María, P.; Miyamoto, K. *Green Chem.* **2011**, *13*, 2607−2618.
(7) Reetz, M. T. *Angew. Chem., Int. Ed.* **2011**, *50*, 138−174.
(8) Kourist, R.; Guterl, J.-K.; Miyamoto, K.; Sieber, V. *ChemCatChem* **2014**, *6*, 689−701.
(9) Terao, Y.; Miyamoto, K.; Ohta, H. *Chem. Lett.* **2007**, *36*, 420−421.
(10) Glavas, S.; Tanner, M. E. *Biochemistry* **2001**, *40*, 6199−6204.
(11) Hwang, K. Y.; Cho, C.-S.; Kim, S. S.; Sung, H.-C.; Yu, Y. G.; Cho, Y. *Nat. Struct. Biol.* **1999**, *6*, 422−426.
(12) Matoishi, K.; Ueda, M.; Miyamoto, K.; Ohta, H. *J. Mol. Catal. B: Enzymol.* **2004**, *27*, 161−168.
(13) Miyamoto, K.; Tsuchiya, S.; Ohta, H. *J. Am. Chem. Soc.* **1992**, *114*, 6256−6257.
(14) Kawasaki, T.; Watanabe, M.; Ohta, H. *Bull. Chem. Soc. Jpn.* **1995**, *68*, 2017−2020.
(15) Okrasa, K.; Levy, C.; Wilding, M.; Goodall, M.; Baudendistel, N.; Hauer, B.; Leys, D.; Micklefield, J. *Angew. Chem., Int. Ed.* **2009**, *48*, 7691−7694.
(16) Okrasa, K.; Levy, C.; Hauer, B.; Baudendistel, N.; Leys, D.; Micklefield, J. *Chem.—Eur. J.* **2008**, *14*, 6609−6613.
(17) Kuettner, E. B.; Keim, A.; Kircher, M.; Rosmus, S.; Sträter, N. *J. Mol. Biol.* **2008**, *377*, 386−394.
(18) Obata, R.; Nakasako, M. *Biochemistry* **2010**, *49*, 1963−1969.
(19) Miyazaki, M.; Kakidani, H.; Hanzawa, S.; Ohta, H. *Bull. Chem. Soc. Jpn.* **1997**, *70*, 2765−2769.
(20) Kourist, R.; Miyauchi, Y.; Uemura, D.; Miyamoto, K. *Chem.—Eur. J.* **2011**, *17*, 557−563.
(21) Terao, Y.; Miyamoto, K.; Ohta, H. *Chem. Commun.* **2006**, 3600−3602.
(22) Terao, Y.; Ijima, Y.; Miyamoto, K.; Ohta, H. *J. Mol. Catal. B: Enzymol.* **2007**, *45*, 15−20.
(23) Ijima, Y.; Matoishi, K.; Terao, Y.; Doi, N.; Yanagawa, H.; Ohta, H. *Chem. Commun.* **2005**, 877−879.
(24) Miyauchi, Y.; Kourist, R.; Uemura, D.; Miyamoto, K. *Chem. Commun.* **2011**, *47*, 7503−7505.
(25) Becke, A. D. *J. Chem. Phys.* **1993**, *98*, 5648−5652.
(26) Lee, C.; Yang, W.; Parr, R. G. *Phys. Rev. B* **1988**, *37*, 785−789.
(27) Frisch, M. J.; Trucks, G. W.; Schlegel, H. B.; Scuseria, G. E.; Robb, M. A.; Cheeseman, J. R.; Montgomery, J. A., Jr.; Vreven, T.; Kudin, K. N.; Burant, J. C.; Millam, J. M.; Iyengar, S. S.; Tomasi, J.; Barone, V.; Mennucci, B.; Cossi, M.; Scalmani, G.; Rega, N.; Petersson, G. A.; Nakatsuji, H.; Hada, M.; Ehara, M.; Toyota, K.; Fukuda, R.; Hasegawa, J.; Ishida, M.; Nakajima, T.; Honda, Y.; Kitao, O.; Nakai, H.; Klene, M.; Li, X.; Knox, J. E.; Hratchian, H. P.; Cross, J. B.; Bakken, V.; Adamo, C.; Jaramillo, J.; Gomperts, R.; Stratmann, R. E.; Yazyev, O.; Austin, A. J.; Cammi, R.; Pomelli, C.; Ochterski, J. W.; Ayala, P. Y.; Morokuma, K.; Voth, G. A.; Salvador, P.; Dannenberg, J. J.; Zakrzewski, V. G.; Dapprich, S.; Daniels, A. D.; Strain, M. C.; Farkas, O.; Malick, D. K.; Rabuck, A. D.; Raghavachari, K.; Foresman, J. B.; Ortiz, J. V.; Cui, Q.; Baboul, A. G.; Clifford, S.; Cioslowski, J.; Stefanov, B. B.; Liu, G.; Liashenko, A.; Piskorz, P.; Komaromi, I.; Martin, R. L.; Fox, D. J.; Keith, T.; Al-Laham, M. A.; Peng, C. Y.; Nanayakkara, A.; Challacombe, M.; Gill, P. M. W.; Johnson, B.; Chen, W.; Wong, M. W.; Gonzalez, C.; Pople, J. A. *Gaussian 03, Revisions D.01, D.02, and E.01*; Gaussian, Inc.: Wallingford, CT, 2004.
(28) Cossi, M.; Rega, N.; Scalmani, G.; Barone, V. *J. Comput. Chem.* **2003**, *24*, 669−681.
(29) Barone, V.; Cossi, M. *J. Phys. Chem. A* **1998**, *102*, 1995−2001.
(30) Grimme, S. *J. Comput. Chem.* **2006**, *27*, 1787−1799.
(31) Siegbahn, P. E. M.; Blomberg, M. R. A.; Chen, S.-L. *J. Chem. Theory Comput.* **2010**, *6*, 2040−2044.
(32) Lonsdale, R.; Harvey, J. N.; Mulholland, A. J. *J. Phys. Chem. Lett.* **2010**, *1*, 3232−3237.
(33) Osuna, S.; Swart, M.; Solà, M. *J. Phys. Chem. A* **2011**, *115*, 3491−3496.
(34) Santoro, S.; Liao, R.-Z.; Himo, F. *J. Org. Chem.* **2011**, *76*, 9246−9252.
(35) Xu, X.; Liu, P.; Lesser, A.; Sirois, L. E.; Wender, P. A.; Houk, K. N. *J. Am. Chem. Soc.* **2012**, *134*, 11012−11025.
(36) Himo, F.; Siegbahn, P. E. M. *J. Biol. Inorg. Chem.* **2009**, *14*, 643−651.
(37) Siegbahn, P. E. M.; Himo, F. *Wiley Interdiscip. Rev.: Comput. Mol. Sci.* **2011**, *1*, 323−336.
(38) Hu, P.; Zhang, Y. *J. Am. Chem. Soc.* **2006**, *128*, 1272−1278.
(39) Senn, H. M.; Thiel, S.; Thiel, W. *J. Chem. Theory Comput.* **2005**, *1*, 494−505.
(40) Senn, H. M.; Kästner, J.; Breidung, J.; Thiel, W. *Can. J. Chem.* **2009**, *87*, 1332−1337.
(41) Blomberg, M. R. A.; Siegbahn, P. E. M. *Biochemistry* **2012**, *51*, 5173−5186.
(42) Miyamoto, K.; Ohta, H.; Osamura, Y. *Bioorg. Med. Chem.* **1994**, *2*, 469−475.
(43) Puig, E.; Mixcoha, E.; Garcia-Viloca, M.; González-Lafont, Á.; Lluch, J. M. *J. Am. Chem. Soc.* **2009**, *131*, 3509−3521.

(44) We also found the transition state for the decarboxylation starting from React-II-*R*1. The barrier was calculated to be 25.6 kcal/mol, that is, 9.4 kcal/mol higher than for React-II-*R*. See the SI for the optimized structure of the transition state.